

Interaction of gypsum with As(V)-bearing aqueous solutions: Surface precipitation of guerinite, sainfeldite, and $\text{Ca}_2\text{NaH}(\text{AsO}_4)_2 \cdot 6\text{H}_2\text{O}$, a synthetic arsenate

JUAN D. RODRÍGUEZ,¹ AMALIA JIMÉNEZ,^{1,*} MANUEL PRIETO,¹ LAURA TORRE,² AND SANTIAGO GARCÍA-GRANDA²

¹Departamento de Geología, University of Oviedo, Jesús Arias de Velasco, Oviedo, Asturias 33005, Spain

²Departamento de Química Física y Analítica, University of Oviedo, Julian Clavería s/n Oviedo, Asturias 33006, Spain

ABSTRACT

The interaction of arsenate-bearing aqueous solutions with gypsum at a starting pH of 9 and 25 °C results in surface precipitation of guerinite, $\text{Ca}_5(\text{HAsO}_4)_2(\text{AsO}_4)_2 \cdot 9\text{H}_2\text{O}$, sainfeldite, $\text{Ca}_5(\text{HAsO}_4)_2(\text{AsO}_4)_2 \cdot 4\text{H}_2\text{O}$, and occasionally $\text{Ca}_2\text{Na}(\text{HAsO}_4)(\text{AsO}_4) \cdot 6\text{H}_2\text{O}$, a new arsenate. These three solid phases are characterized by the simultaneous presence of HAsO_4^{2-} and AsO_4^{3-} groups in their structure, which is explainable since crystallization occurs within a pH range in which both HAsO_4^{2-} and AsO_4^{3-} are available in the aqueous solution. The interaction leads to a decrease in the As(V) concentration in the aqueous phase to reach values controlled by the solubility of these solid phases. The study combines several macroscopic experiments, in which changes in the solution chemistry are monitored as a function of time, with the characterization of solid phases by SEM-EDS and XRD. The crystal morphologies of the precipitating phases are interpreted on the basis of their respective structures. The thermodynamic solubility products of both guerinite and the new arsenate have been determined, being $10^{-31.17 \pm 0.05}$ and $10^{-13.83 \pm 0.03}$, respectively. The reaction paths followed by the system and the equilibrium endpoints have been modeled using the geochemical code PHREEQC.

Keywords: Crystal growth, calcium arsenate, analysis chemical, sainfeldite, phase equilibrium, guerinite, gypsum

INTRODUCTION

Although the mobility and toxicity of As in the environment have been studied extensively (Smedley and Kinniburgh 2002; Vaughan 2006), numerous issues remain unresolved. On the one hand, it is well established that under oxidizing conditions, As(V) is the most common form of As in natural waters, with AsO_4^{3-} , HAsO_4^{2-} , $\text{H}_2\text{AsO}_4^{1-}$, and H_3AsO_4^0 being the prevailing aqueous species in different pH ranges. On the other hand, the crystal chemistry and thermodynamic properties of arsenates remain largely unknown. Moreover, with some significant exceptions (Bothe and Brown 1999a; Lee and Nriagu 2007), the determination of thermodynamic solubility products of arsenates has received little attention, perhaps as a consequence of the complicated crystallization behavior of these compounds in aqueous environments, which involves formation of an enormous diversity of hydrates, double salts, the presence of arsenate groups with different protonation degrees, etc. This lack of data is an important handicap because an in-depth study of arsenate mobility in natural systems requires a precise knowledge of the solid phases that may or may not precipitate their crystal chemistry and their solubility.

Immobilization of arsenate in the environment can occur by precipitation of low-solubility salts or by sorption on mineral surfaces in soils, sediments, and aquifers. Artificial remedia-

tion methods are based on the same mechanisms, and the most common techniques are precipitation by reaction with suitable chemicals and sorption (e.g., Nishimura et al. 2000 and references therein). This last term describes various mechanisms (Sposito 1986), including true adsorption, absorption, or diffusion into the solid, and surface precipitation to form a crystalline, adherent phase that may consist of chemical species derived from both the aqueous solution and the dissolution of the solid. Regarding arsenate sorption, most of the research has focused on adsorption onto clays (e.g., Frost and Griffin 1977; Manning and Goldberg 1996), sulfides (Farquhar et al. 2002), and hydrous metal oxides of Al, Mn, and Fe (e.g., Pierce and Moore 1982; Driehaus et al. 1995; Foster et al. 1998). However, even though these adsorption phenomena can be an efficient As sink, desorption is a relatively rapid process that must also be considered, and the selection of sorptive remediation materials has to be done bearing in mind the possibility of remobilization (O'Reilly et al. 2001).

Sorption by surface precipitation of arsenates on carbonate minerals is also a possibility, and the interaction of As(V) with limestone has been widely studied in the literature (e.g., Brannon and Patrick 1987; Bothe and Brown 1999b; Twidwell et al. 1999 and references therein). This interaction leads to the formation of a series of Ca-arsenate compounds, many of them with unknown XRD patterns, whose compositions have not been completely established (Swash and Monhemius 1995). At present there are over 20 different Ca-arsenate compounds in the Powder Diffraction File, but the crystal structure has only been determined

* E-mail: amalia.jimenez@geol.uniovi.es

for 11 of these compounds. The most complete research on the crystal chemistry of these arsenates was carried out during the seventies by Ferraris and co-workers, who studied the structures of CaHAsO_4 (weilite), $\text{CaHAsO}_4 \cdot 2\text{H}_2\text{O}$ (pharmacolite), $\text{CaHAsO}_4 \cdot \text{H}_2\text{O}$ (haidingerite), $\text{Ca}_5(\text{HAsO}_4)_2(\text{AsO}_4)_2 \cdot 9\text{H}_2\text{O}$ (guerinite and ferrarisite), $\text{Ca}_5(\text{HAsO}_4)_2(\text{AsO}_4)_2 \cdot 4\text{H}_2\text{O}$ (sainfeldite), and other arsenates and H arsenates of Ca (Ferraris et al. 1971, 1972; Ferraris and Chiari 1970; Catti and Ferraris 1974; Catti et al. 1980; Ferraris and Abbona 1972). Bothe and Brown (1999a) identified and determined the solubility products of several arsenates of low solubility, including $\text{Ca}_4(\text{OH})_2(\text{AsO}_4)_2 \cdot 4\text{H}_2\text{O}$, $\text{Ca}_5(\text{AsO}_4)_3\text{OH}$, and $\text{Ca}_3(\text{AsO}_4)_2 \cdot 3^{2/3}\text{H}_2\text{O}$. Unfortunately, these insoluble Ca arsenates crystallize at high pH values. At a pH < 8, there is a tendency to form more-soluble, hydrated acidic arsenates, which are unlikely to produce aqueous solutions with As concentrations below the guideline values proposed for As dissolved in potable water (Magalhães 2002). Moreover, there is also strong evidence that Ca-arsenate compounds of low solubility are not stable in the presence of air at a pH > 8 (Robins 1981; Nishimura et al. 1983). Carbon dioxide in air will convert the Ca arsenate to Ca carbonate with the subsequent release of As back into the aqueous phase.

In addition to Ca arsenates, several metal-arsenates and mineral-like arsenates (e.g., Jiménez et al. 2004; Twidwell et al. 1999 and references therein) have been proposed as possible immobilizing phases, but the solubility and the precise identity and structure of these phases is in many cases not known. The obvious conclusion is that research on the structure, solubility, and crystallization behavior of new arsenate-containing materials has to be conducted. Roman-Ross and co-workers (Roman-Ross et al. 2003; Fernández-Martínez et al. 2006) have recently studied the precipitation of gypsum by mixing CaCl_2 and Na_2SO_4 aqueous solutions in the presence of dissolved Na_2HAsO_4 , and have detected the incorporation of some arsenate (substituting for sulfate) into the gypsum structure. This incorporation supposes an increase of the unit-cell parameters, as AsO_4^{3-} (or HAsO_4^{2-}) is greater than SO_4^{2-} . In conclusion, these authors suggested that As(V) could be sorbed onto gypsum by forming a limited Ca-arsenate-sulfate solid solution. In fact, surface precipitation of pollutant-bearing solid solutions has been found to be a significant, long-term mechanism of sorption not only of cations but also of oxyanions (Prieto et al. 2002; Andara et al. 2005; Fernández-González et al. 2006) on carbonates and sulfates. The existence of a certain connection between arsenate and gypsum has also been documented by Juillot et al. (1999), who, in studying the remobilization of As from buried wastes at an industrial site, observed an intimate association of gypsum and Ca arsenates, detecting that gypsum may contain some As and that Ca arsenates may contain some S. However, to our knowledge there are no studies in the literature quantifying the uptake behavior of arsenate on gypsum.

In this work, we have studied the interaction of Na_2HAsO_4 aqueous solutions with gypsum, to check the effectiveness of this mineral in removing As from water within a moderately basic pH range (<9). To this aim, we have combined several macroscopic techniques, in which changes in the solution chemistry have been monitored as a function of time, with microscopic observations and X-ray diffraction (XRD). We find that the for-

mation of arsenate-bearing gypsum (with arsenate substituting for sulfate in the structure) has a negligible effect on the solution composition, with the removal of As mostly occurring by surface precipitation of guerinite, sainfeldite, and a new arsenate, $\text{Ca}_2\text{Na}(\text{HAsO}_4)(\text{AsO}_4) \cdot 6\text{H}_2\text{O}$. Although gypsum does not seem to be a suitable remediation tool at pH <9, the nature, solubility, and crystallization behavior of the solid phases that precipitate in this pH range need to be investigated. In this framework, our study proposes an estimation of the solubility product at 25 °C and 1 atm for both guerinite and the new arsenate, as well as a model for the reaction paths followed by the system.

EXPERIMENTAL METHODS

Interaction experiments

Interaction experiments were carried out at 25 ± 0.1 °C and at atmospheric pressure by reacting gypsum grains with Na_2HAsO_4 aqueous solutions in thermostated and continuously stirred (100 rpm) polypropylene vessels. In most of the experiments, 2 g of mineral grains with diameters ranging from 1.0 to 1.5 mm were added to 100 cm³ of reacting solution. Moreover, to check the grain size effect, one set of experiments was performed with solids ranging from 0.5 to 1.0 mm in diameter. Gypsum grains were obtained by crushing natural single crystals. The resultant fragments were sieved to the selected size range and ultrasonically cleaned in an ethanol bath. This starting material was confirmed to be gypsum by X-ray diffraction (XRD, Philips-X'Pert-PRO) and analyzed by X-ray fluorescence spectroscopy (XRF, Philips-PW2404). XRF analyses yielded less than 0.2 wt% foreign elements, with Na, Sr, and P as major impurities. The grains are essentially cleavage fragments dominated by (010) crystal faces, with a specific N_2 -BET (Micrometrics-ASAP-2010) surface area of 0.16 m²/g (0.22 m²/g for the grains with diameters in the range 0.5–1.0 mm). The use of cleavage fragments with smooth surfaces within this size range minimized the significance of adsorption in comparison with surface precipitation.

For each starting solution (100, 50, 25, 20, 10, 5, and 2 mM of arsenate), a set of experiments with increasing reaction times was carried out. The experiments were performed by placing 100 cm³ (weighed to 0.001 g) of solution and 2.000 ± 0.005 g of gypsum grains in the reacting vessel. The starting solutions were prepared with reagent grade $\text{Na}_2\text{HAsO}_4 \cdot 7\text{H}_2\text{O}$ (Merck) and deionized water (MilliQ System) at ambient CO₂ partial pressure. The vessels were then closed with polypropylene caps to avoid contact with the atmosphere and minimize evaporation during the experiments. After the corresponding reaction period, the experiment was stopped and the solution was assayed for dissolved Ca, sodium, sulfate, As, and pH. Concentrations and pH evolution were monitored in this way for 50 days. Each experiment was repeated three times. Thus, the reported results are the average value of three analogous experiments. The solution pH was measured with a combination electrode (Ross-Thermo-Orion-810200) and a digital pH-meter (CyberScan-pH-2100). Multipoint calibration of the electrode was performed with 4.01, 7.00, and 10.01 NIST-traceable buffers (Thermo-Orion). Dissolved As was determined by Inductively Coupled Plasma Optical Emission Spectroscopy (ICP-OES, Perkin-Elmer-Optima-3300-DV). Calcium and Na were measured by Atomic Absorption Spectrometry (AAS, Pye-Unicam-SP-90); dissolved sulfate was analyzed by ion chromatography (IC, Metrohm Compact IC 761). The results are reproducible, particularly in the case of As. The variation in As concentration from replicate experiments at the same reaction time was always less than ±4% (RSD). For Ca, Na, and sulfate this variation was found to be within ±8% (RSD), ±6%, and ±5%, respectively. Speciation and aqueous solution modeling was carried out using the geochemical code PHREEQC (Parkhurst and Appelo 1999), a geochemical modeling program based on the ion-association aqueous model with a diversity of capabilities.

Characterization of the solid phases

After the experimental runs, representative individuals of the gypsum crystals were selected from the aqueous solution to verify the incorporation of As-bearing phases on their surfaces. For this purpose, the samples (the gypsum grains with the corresponding overgrowth) were carbon-coated and then examined with a scanning electron microscope (SEM, JEOL-JSM-6100). This SEM was also used to estimate the composition of the precipitates using an INCA Energy 200 microanalysis system (EDS) with a silicon detector (PentaFET, Oxford Instruments) fitted

with an ultra-thin window that allows the detection of O. SEM-observations were combined with an XRD study (Philips-X-Pert-PRO) to complete the characterization of the precipitate layer. To avoid the inclusion of peaks from the substrate, the diffraction patterns were obtained by carrying out 2 θ scans (from 3 to 45°) at a fixed small angle of incidence (3 or 4° depending on the sample) on the substrate surface. The diffractograms obtained in this way involve essentially the precipitate overgrowth and only in some cases include the most intense peaks corresponding to the underlying gypsum.

Starting from a 100 mM As(V) parent solution, some tiny crystals of an unknown phase appeared in the early stages of the experiment (see the section of results). To obtain samples of this phase suitable for characterization by single-crystal XRD, specific crystallization experiments were carried out by mixing CaCl₂ (0.01 mM) and Na₂HAsO₄ (1 M) aqueous solutions in a thermostated (25 ± 0.1 °C) polypropylene vessel. 50 cm³ of each parent solution were placed in the reacting vessel, which was then sealed with a polypropylene cap to avoid evaporation. Following mixing, the solution pH reached a value of ~8.90. After several days of growth, the resultant crystals (~100 μm) were extracted and studied by single-crystal XRD. The structure was solved by Patterson methods, using the program DIRDIF-99 (Beurskens et al. 1992). Experimental details on the crystal-structure determination of this new phase can be seen in Jiménez et al. (2006). Moreover, to determine the solubility of this unknown phase, the evolution of both solution pH and composition was monitored over 1800 h.

RESULTS

Uptake of As, release of Ca, and pH evolution

Figure 1 shows the evolution of As and Ca concentrations as a function of time for the experimental series carried out with a 25 mM parent solution and grain sizes in the range 1–1.5 mm. As can be observed, the As concentration decreases quickly during the first 24 h. This decrease goes with an increase in the Ca and sulfate concentration and a reduction of pH (see inset in Fig. 1). The result is similar in the experiments carried out starting from 100, 50, 20, and 10 mM Na₂HAsO₄ parent solutions, in which two consecutive stages were observed: the As concentration falls rapidly in the early hours of the experiment and then evolves slowly toward an asymptotic value (As_{∞} in Table 1). In contrast, in the experiments carried out starting from less-concentrated (5 and 2 mM) aqueous solutions, the decrease is negligible or within the experimental uncertainties.

Table 1 shows the concentration of Na₂HAsO₄ added in the parent dissolution (As_0) and the concentration of As (As_{∞}) mea-

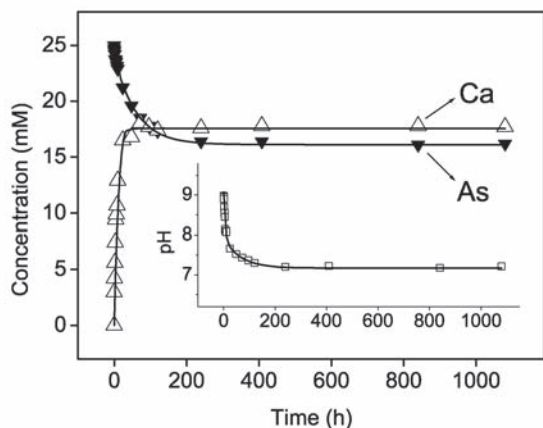


FIGURE 1. Evolution of As and Ca concentrations as a function of time. The inset shows the corresponding evolution of pH. Parent solution: 25 mM Na₂HAsO₄. Grain size: 1.0 < ϕ < 1.5 mm.

sured at the end (50 days) of the experiments. The total uptake (U_{∞}) of As per gram of gypsum is given by

$$U_{\infty} = (As_0 - As_{\infty})/20 \quad (1)$$

where $As_0 - As_{\infty}$ equals the number of millimoles of As removed from one liter of solution, and the factor 20 is the weight of mineral solids per liter (i.e., 2 g in 100 cm³). Finally, the columns U_{∞}/S_{BET} and U_{∞}/S_{gsa} represent the total uptake normalized to the specific BET-surface area and to the specific “geometric-surface” area, respectively. This last parameter was estimated by assuming that all grains were identically sized, smooth cubes (Oelkers 1996) using

$$S_{gsa} = 6/ap \quad (2)$$

where a represents cube edge length and ρ stands for the solid density. For the gypsum grains used here, the specific geometric-surface area was 0.021 m²/g (0.035 m²/g for the grains with diameters in the range 0.5–1.0 mm). Geometric surface areas are related to BET surface areas through a surface roughness parameter, $R = S_{BET}/S_{gsa}$, which in this case was ~7.6 (6.3 for 0.5–1.0 mm), a low value that confirms the smoothness of the involved surfaces.

As can be observed, the amount of As precipitated on the solids (U_{∞} in Table 1) increases as the concentration of the starting solution increases. The effect is also clear when the values are normalized to the surface area. An important aspect at this point is related to the grain-size effect on the uptake process. To establish this effect, two sets of experiments with the same As concentration (25 mM) but using gypsum grains within different size ranges (1.0–1.5 and 0.5–1.0 mm) have been performed. As can be observed, the amount of As removed from the fluid is similar in both cases, which is in relation with the type of sorption mechanism (surface precipitation) involved (see discussion section). Since the surface area of the grains with smaller size is obviously higher, the surface-normalized uptake of As is quite lower ($U_{\infty}/S_{BET} = 2.05$ mmol/m² and $U_{\infty}/S_{gsa} = 12.9$ mmol/m²) in this case. This does not mean that the reactive surface area is irrelevant for the process. Although the final amount of As removed from the fluid is similar in both cases, the kinetics is different. This can be observed in Figure 2, where the decrease of As concentration is shown to be faster in the case of the grains with smaller size.

The solutions were prepared at ambient CO₂ partial pressure, the initial water having a pH of ~5.6. After adding the solute (Na₂HAsO₄·7H₂O), the pH increases to reach an initial value that depends slightly on the solute concentration. Then, in the

TABLE 1. Uptake of As (asymptotic values)

As_0 (mM)	As_{∞} (mM)	U_{∞} (mmol/g ¹)	U_{∞}/S_{BET} (mmol/m ²)	U_{∞}/S_{gsa} (mmol/m ²)
100	62.5	1.88	11.8	89.5
50	31.2	0.94	5.88	44.5
25	16.2	0.44	2.75	21.0
25 (small size)	16.1	0.45	2.05	12.9
20	13.9	0.31	1.94	14.8
10	9.4	0.03	0.19	1.43
5	~5	–	–	–
2	~2	–	–	–

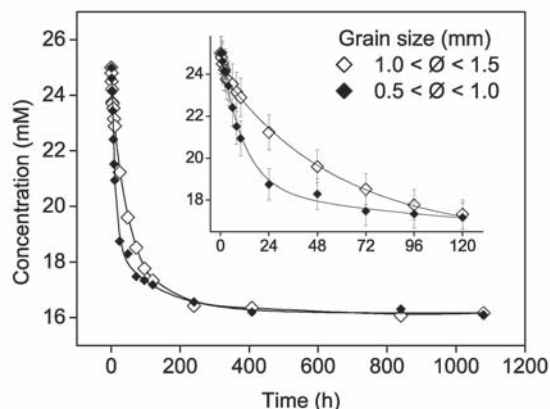


FIGURE 2. Effect of grain size on the evolution of As concentration. The inset shows a detail corresponding to the first 5 days of the experiment. Parent solution: 25 mM Na_2HAsO_4 .

course of the interaction with the gypsum crystals, the solution pH slowly decreases toward an asymptotic value, following a trend parallel to the decrease of the As concentration (see Fig. 1). Table 2 shows the initial solution pH (pH_0) and the value measured at the end of the experiments (pH_∞). For the experiments carried out with 100, 50, 25, 20, and 10 mM solutions, the pH decreases during the first 24 h from an initial value of ~ 9.0 to a value < 7.5 , approaching a lower asymptotic value for prolonged reaction times. Starting from less-concentrated solutions (5 and 2 mM), the pH decreases a few tenths in the beginning of the experiment, then remains virtually constant.

The increase in Ca concentration is obviously a consequence of the gypsum dissolution, which is common in all the experiments. At the beginning of every experiment, the aqueous solution is free of Ca, but the concentration of this element increases rapidly during the first ~ 24 h and rises slowly afterward, approaching an asymptotic value for prolonged reaction times (see Ca_∞ in Table 2). The concentration of sulfate (S_∞ in Table 2) increases in a similar way, but it is always higher than that of Ca. As noted below, this feature is due to the fact that a part of the released Ca is consumed during the process by precipitation of Ca-bearing solid phases. In contrast, the concentration of Na remains virtually constant (deviations are in the rank of the experimental uncertainties) during the experiments. Only in the case of the experiments carried out in 100 mM parent solutions do the deviations seem to reach noticeable values. Figure 3 shows the evolution of Na concentration for the experiments carried out starting from this parent solution. As can be observed, there is a clear decrease in concentration during the first 6–8 h of the experiment and a slow rise afterward, that eventually reaches the initial value. In this figure, the data-points represent the mean of three replicate experiments and clearly confirm the existence of a transitory but very reproducible decrease in As concentrations.

Microscopic characterization of the solids

Figure 4a shows the surface of a typical gypsum grain after 18 h of reaction with a 50 mM parent solution. The surface shows dissolution signs and is covered by a precipitate consisting of

TABLE 2. Concentration of Ca, sulfate and pH level after prolonged reaction times

Parent solution Na_2HAsO_4 (mM)	Ca_∞ (mM)	S_∞ (mM)	pH_0	pH_∞
100	15.5	62.3	8.9	7.0
50	16.4	40.0	8.9	7.1
25	17.9	29.1	9.0	7.2
25 (small size)	17.8	28.9	9.0	7.2
20	18.5	25.7	9.0	7.2
10	18.6	19.3	9.0	7.5
5	16.1	16.2	9.0	8.7
2	15.5	15.2	8.9	8.8

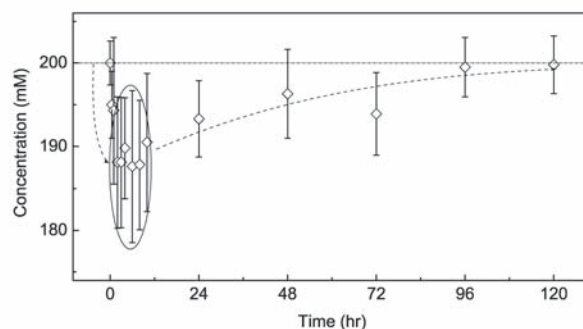


FIGURE 3. Sodium concentration as a function of time. Parent solution 100 mM Na_2HAsO_4 . Grain size: $1.0 < \phi < 1.5$ mm.

aggregates of small ($\sim 30 \mu\text{m}$) crystals with lamellar morphologies (Fig. 4b). The precipitate begins to grow at the cleavage steps of the grain perimeters and extends to quickly cover the (010) gypsum surface, which becomes completely covered by a crust of precipitate after 24 h of reaction. The precipitate features are similar in the experimental series carried out with a 25 mM parent solution, but in this case the nucleation density is lesser and the crystallites reach larger (up to $\sim 100 \mu\text{m}$) sizes. Although EDS microanalyses of this kind of flaky crystals are approximate, our measurements systematically suggest atomic Ca/As ratios slightly higher than unity. This observation is in good agreement with the presence of the main reflections of guerinite (at $d \sim 14.1$, 3.90, 2.91 \AA , etc.) in the diffractograms.

Guerinite is a Ca arsenate in which unprotonated AsO_4^{3-} and monoprotonated arsenate HAsO_4^{2-} groups coexist to form a nonahydrate, $\text{Ca}_5(\text{HAsO}_4)_2(\text{AsO}_4)_2 \cdot 9\text{H}_2\text{O}$, with monoclinic, $P2_1/n$, structure. The crystal structure of guerinite is characterized by $(\bar{1}01)$ layers built up by $[\text{AsO}_4]$ tetrahedra linked to Ca polyhedra (N.C. 7 or 8) by sharing vertices and edges (Catti and Ferraris 1974). An H-bonding system connects these $(\bar{1}01)$ layers between them, both the water H atoms and the anionic H atoms being involved in the H bridges. Two of the five independent Ca polyhedra share faces and form chains along the [010] direction. These structural features are consistent with the morphological characteristics observed in the precipitated guerinite crystals. Figure 5 shows the typical morphology, which consists of thin lamellar sheets elongated on the b axis. These sheets correspond to $\{\bar{1}01\}$ pinacoids, defined by the crystallographic planes with the highest d -spacing (14.1 \AA).

Using a 20 mM parent solution, the isolated aggregates grow and cover less than 20% of the surface after prolonged reaction times. In this case, a detailed observation of the precipitate al-

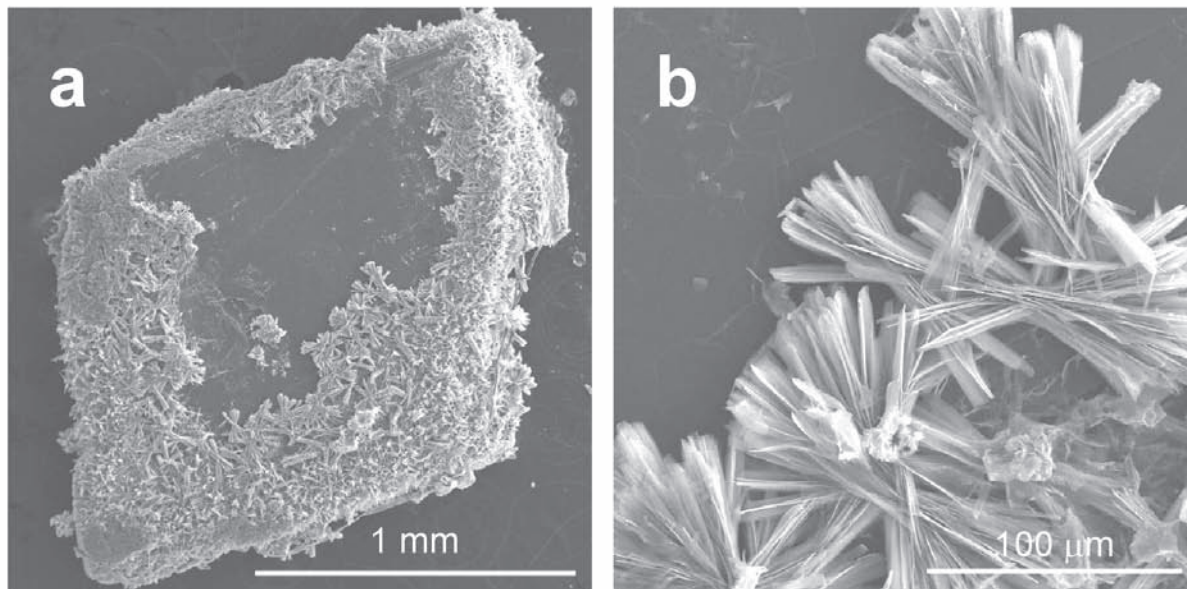


FIGURE 4. Surface of a typical gypsum grain after 18 h of reaction with a 50 mM parent solution. (a) Overall grain aspect. The original surface is covered by crystalline aggregates formed by individuals with laminar shapes. (b) Precipitate aspect at a higher magnification.

lows discerning between two different kinds of crystals, G and S (Fig. 6), with laminar and prismatic shapes, respectively. The laminar crystals are analogous (morphology and EDS analyses) to those shown in Figures 4b and 5, which were identified as guerinite. This analogy is in agreement with the presence of the main reflections of guerinite in the diffractograms, which firmly supports the identification of the crystals labeled G as this mineral. The crystals labeled S show an elongated shape with well-defined crystal faces. EDS analyses yield Ca/As atomic ratios similar to that observed in the laminar crystals identified as guerinite. However, both O/Ca and O/As atomic ratios were systematically determined to be significantly lower than that of guerinite, within the unavoidable experimental error. Both ratios point to the sainfeldite stoichiometry, $\text{Ca}_5(\text{HAsO}_4)_2(\text{AsO}_4)_2 \cdot 4\text{H}_2\text{O}$, which is in agreement with the presence of the main reflections of this mineral (at $d \text{ \AA} \sim 8.7, 4.67, 3.88, \text{ and } 3.18$) in the diffractograms.

In a similar way to guerinite, AsO_4^{3-} and HAsO_4^{2-} groups coexist in sainfeldite to form a Ca-arsenate hydrate with monoclinic ($C2/c$) structure (Ferraris and Abbona 1972). The arsenate groups are linked to irregular $[\text{CaO}_6]$ octahedra to form a three-dimensional framework with channels along $[001]$, where the water molecules, which are Ca-coordinated, are located. These molecules, as well as the acidic H atoms of the HAsO_4^{2-} groups, are involved in H bonds that reinforce the structure, especially along $[001]$. Moreover, different periodic bond chains (PBCs) involving As-O-Ca links can be discerned within the polyhedral framework, of which those along $[001]$ seem to be particularly strong. An in-depth study of PBCs is, however, beyond the scope of the present work.

Figure 6 illustrates the typical morphology of these crystals, which consists of two four-faced prisms, $\{11\bar{1}\}$ and $\{110\}$, and the front $\{100\}$ pinacoid. These three forms correspond to the crystallographic planes with the highest d -spacings (6.78, 8.69,

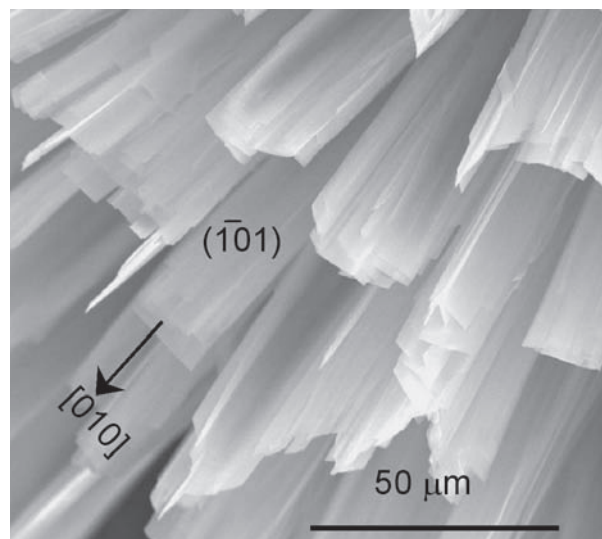


FIGURE 5. Guerinite crystals on the surface of a gypsum grain. The crystals show laminar shapes corresponding to $\{1\bar{1}0\}$ pinacoids and are elongated on $[010]$.

and 9.32 \AA , respectively) and were expected to be among the most important growth forms of sainfeldite. In fact, the crystal habit in Figure 6c has been simulated using the Donnay-Harker (D-H) tool of the computer code SHAPE (V7.1.2, Shape Software 2004), according to the following equation (Dowty 1980):

$$RG_{hkl} = d_{hkl} \exp(-kd_{hkl}) \quad (3)$$

where k is a semiempirical constant that depends on a set of different crystal-growth parameters, including surface energy and supersaturation. RG_{hkl} is the linear growth rate of the (hkl) crystal

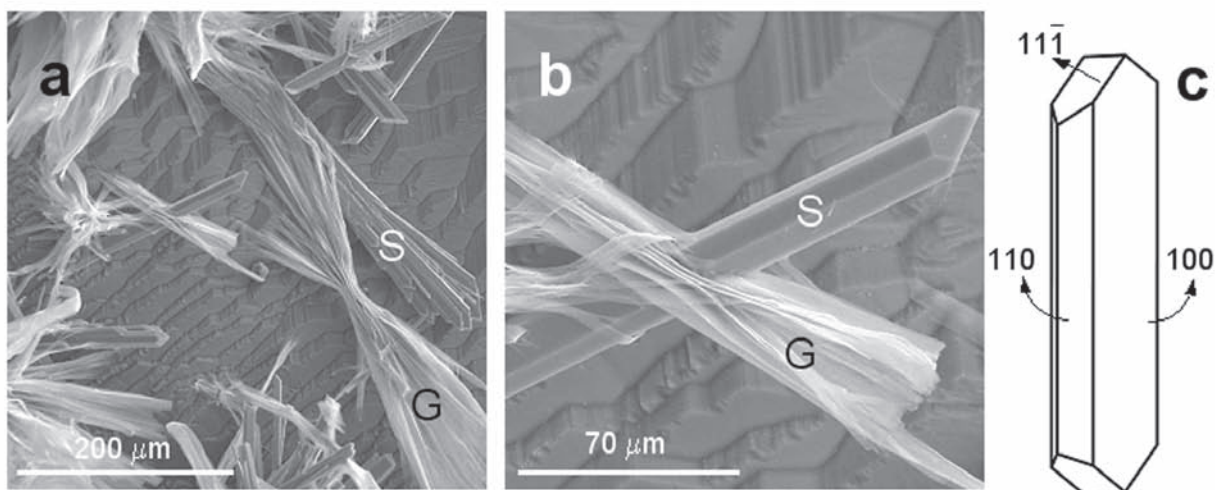


FIGURE 6. Surface of a typical gypsum grain after several days of reaction with a 20 mM Na_2HAsO_4 parent solution. (a) Guerinite (G) and sainfeldite (S) crystals on the gypsum surface. (b) Detail at a higher magnification. (c) Habit of a sainfeldite crystal simulated according to Equation 3.

face and d_{hkl} the spacing of the corresponding crystallographic plane, derived according to the Donnay-Harker (1937) rules. Of course, this model is a simplification, but the D-H list as derived by SHAPE can be useful as a ranking of forms in order of probability of occurrence. In this case, the best fit with the observed morphology was obtained for $k = 0.6$. As can be observed, the crystal is elongated along [001] and the most developed forms, {110} and {100}, belong to the [001] zone. Both features are in agreement with the presence of an important set of PBCs along [001] in the sainfeldite structure. Finally, in contrast to guerinite, the structure of sainfeldite explains the lack of clear cleavage planes in the precipitated crystals.

The experimental series performed starting from a 100 mM parent solution needs a separate mention due to the presence of specific features not observed in the experiments carried out with less concentrated parent solutions. Whereas the final precipitate consists entirely of guerinite crystals, during the early hours of the experiment, some aggregates of a different nature nucleate on the gypsum surface. These aggregates seem to be transitory and begin to dissolve and completely disappear after two days of reaction, being substituted by guerinite. Unfortunately, it was not possible to carry out an effective compositional characterization of these aggregates by SEM-EDS, due to their small size ($<2 \mu\text{m}$) with respect to the electron beam. Whereas Na and As seem to be two important constituents of this phase, the amount of Ca is difficult to assess as the analyses are contaminated by the underlying gypsum substrate and are quite uncertain.

With the aim of characterizing this transitory phase, a separate crystallization experiment has been performed (see experimental section). The idea was to reproduce the conditions at the early stages of the 100 mM interaction experiment, i.e., a basic pH (around 9), a very high concentration of Na_2HAsO_4 , and a low concentration of Ca. To avoid the subsequent evolution of the system, the experiment was performed without the presence of gypsum grains simply by mixing CaCl_2 and Na_2HAsO_4 aqueous solutions. The crystallization conditions were optimized after several trial-and-error runs using different initial concentrations.

After a while, a precipitate of microcrystals began to develop and was left to grow over a period of 10 days. The resultant crystals exhibit tabular shapes ($\sim 150 \mu\text{m}$) with well-defined polygonal contours and unknown powder diffraction patterns. Single-crystal XRD indicates that this phase is $\text{Ca}_2\text{Na}(\text{HAsO}_4)(\text{AsO}_4) \cdot 6\text{H}_2\text{O}$ (Jiménez et al. 2006). Moreover, EDS-analyses of several suitable crystals (over $10 \mu\text{m}$ thick) indicate the presence of Na, Ca, As, and O. These crystals exhibit the same habit and essentially the same composition as those obtained in the interaction experiments. Therefore, it is reasonable to assume that both crystal families correspond to the same phase. The mean Ca/As and Na/As atomic ratios are, respectively, close to 1 and 0.5. Finally, within the unavoidable experimental error, the O/As ratio has a mean value around 7. These mean ratios point to a hydrated double-arsenate of Ca and Na, $\text{Ca}_2\text{Na}(\text{HAsO}_4)(\text{AsO}_4) \cdot 6\text{H}_2\text{O}$, which is in agreement with the data obtained from the structural determination (Jiménez et al. 2006). The coexistence of acidic HAsO_4^{2-} and plain arsenate AsO_4^{3-} groups is analogous to that observed in guerinite and sainfeldite, and is explainable if one considers that crystallization occurs within a pH range in which both HAsO_4^{2-} and AsO_4^{3-} ions are available in the aqueous solution. As the crystal structure of this new arsenate has not yet been described in a detailed way, we include here a description of the different types of polyhedra, their links to neighboring polyhedra, and other structural peculiarities. The crystal morphology is interpreted on this basis.

Structure and morphology of $\text{Ca}_2\text{Na}(\text{HAsO}_4)(\text{AsO}_4) \cdot 6\text{H}_2\text{O}$, a new arsenate

This new compound crystallizes in the triclinic space group $P\bar{1}$, with $a = 6.680 \text{ \AA}$, $b = 8.223 \text{ \AA}$, $c = 12.537 \text{ \AA}$, $\alpha = 73.46^\circ$, $\beta = 78.89^\circ$, and $\gamma = 87.47^\circ$, and two formula units per unit cell (Jiménez et al. 2006). Selected interatomic distances and bond angles derived for this phase are shown in Tables 3 and 4. Figure 7 shows a projection of the structure onto (010). The structure is formed by layers parallel to (001) consisting of $[\text{AsO}_4]$ tetrahedra and $[\text{CaO}_6]$ polyhedra. These layers are linked to each other by

TABLE 3. Atomic distances (Å) for $\text{Ca}_2\text{NaH}(\text{AsO}_4)_2 \cdot 6\text{H}_2\text{O}$

AsO_4 tetrahedra	Calcium octahedra	Sodium octahedra	Water molecules
$\text{As}_1\text{-O}_8 = 1.715$	$\text{Ca}_3\text{-O}_7 = 2.298$	$\text{Na-O}_{15} = 2.395$	$\text{O}_{12}\text{-H}_{12A} = 1.000$
$\text{As}_1\text{-O}_9 = 1.652$	$\text{Ca}_3\text{-O}_{11} = 2.352$	$\text{Na-O}_8 = 2.425$	$\text{O}_{12}\text{-H}_{12B} = 0.998$
$\text{As}_1\text{-O}_{10} = 1.656$	$\text{Ca}_3\text{-O}_9 = 2.367$	$\text{Na-O}_{18} \text{ no. 7} = 2.478$	$\text{O}_{15}\text{-H}_{15A} = 1.002$
$\text{As}_1\text{-O}_{20} = 1.664$	$\text{Ca}_3\text{-O}_{20} \text{ no. 3} = 2.385$	$\text{Na-O}_{18} = 2.478$	$\text{O}_{15}\text{-H}_{15B} = 1.002$
	$\text{Ca}_3\text{-O}_{11} \text{ no. 4} = 2.412$	$\text{Na-O}_{16} = 2.517$	$\text{O}_{16}\text{-H}_{16A} = 1.002$
$\text{As}_2\text{-O}_7 = 1.684$	$\text{Ca}_3\text{-O}_{17} = 2.435$	$\text{Na-O}_{16} \text{ no. 6} = 2.517$	$\text{O}_{16}\text{-H}_{16B} = 1.002$
$\text{As}_2\text{-O}_{11} \text{ no. 1} = 1.689$			$\text{O}_{17}\text{-H}_{17A} = 0.999$
$\text{As}_2\text{-O}_{14} \text{ no. 2} = 1.665$	$\text{Ca}_4\text{-O}_{14} = 2.275$		$\text{O}_{17}\text{-H}_{17B} = 1.002$
$\text{As}_2\text{-O}_{13} = 1.672$	$\text{Ca}_4\text{-O}_{10} = 2.331$		$\text{O}_{18}\text{-H}_{18A} = 1.002$
	$\text{Ca}_4\text{-O}_9 \text{ no. 3} = 2.360$		$\text{O}_{18}\text{-H}_{18B} = 1.002$
	$\text{Ca}_4\text{-O}_{10} \text{ no. 5} = 2.417$		$\text{O}_{19}\text{-H}_{19A} = 1.002$
$\text{O}_{13}\text{-H}_{13} = 0.62$	$\text{Ca}_4\text{-O}_7 \text{ no. 5} = 2.447$		$\text{O}_{19}\text{-H}_{19B} = 1.002$
	$\text{Ca}_4\text{-O}_{12} = 2.481$		

Notes: no. 1 = $x + 1, +y, +z$; no. 2 = $x, +y - 1, +z$; no. 3 = $-x + 1, -y, -z + 1$; no. 4 = $-x + 1, -y + 1, -z + 1$; no. 5 = $-x, -y, -z + 1$; no. 6 = $-x + 1, -y, -z + 2$; no. 7 = $-x, -y, -z + 2$.

TABLE 4. Selected bond angles ($^\circ$) for $\text{Ca}_2\text{NaH}(\text{AsO}_4)_2 \cdot 6\text{H}_2\text{O}$

AsO_4 tetrahedra	Calcium octahedra	Sodium octahedra
$\text{O}_9\text{-As}_1\text{-O}_{10} = 108.2$	$\text{O}_{20}\text{-Ca}_3\text{-O}_{11} \text{ no. 3} = 170.3$	$\text{O}_{16}\text{-Na-O}_{18} = 96.4$
$\text{O}_9\text{-As}_1\text{-O}_{20} = 113.3$	$\text{O}_7\text{-Ca}_3\text{-O}_{17} = 152.7$	$\text{O}_{16}\text{-Na-O}_{15} = 96.25$
$\text{O}_9\text{-As}_1\text{-O}_8 = 108.1$	$\text{O}_7\text{-Ca}_3\text{-O}_{20} \text{ no. 3} = 95.5$	$\text{O}_{18}\text{-Na-O}_{15} = 166.1$
$\text{O}_{10}\text{-As}_1\text{-O}_{20} = 114.3$	$\text{O}_7\text{-Ca}_3\text{-O}_{17} = 82.2$	$\text{O}_{16}\text{-Na-O}_8 = 169.6$
$\text{O}_{10}\text{-As}_1\text{-O}_8 = 107.3$	$\text{O}_7\text{-Ca}_3\text{-O}_{20} \text{ no. 3} = 85.9$	$\text{O}_{18}\text{-Na-O}_8 = 84.4$
$\text{O}_{20}\text{-As}_1\text{-O}_8 = 105.1$	$\text{O}_{11}\text{-Ca}_3\text{-O}_{17} = 105.4$	$\text{O}_{15}\text{-Na-O}_8 = 84.2$
$\text{O}_{14}\text{-As}_2\text{-O}_{13} \text{ no. 2} = 109.7$	$\text{O}_7\text{-Ca}_4\text{-O}_{12} = 152.1$	
$\text{O}_{14}\text{-As}_2\text{-O}_7 \text{ no. 2} = 112.8$	$\text{O}_9\text{-Ca}_4\text{-O}_{10} \text{ no. 3} = 148.2$	
$\text{O}_{13}\text{-As}_2\text{-O}_7 = 111.1$	$\text{O}_9\text{-Ca}_4\text{-O}_7 \text{ no. 3} = 128.8$	
$\text{O}_{14}\text{-As}_2\text{-O}_{11} \text{ no. 2} = 109.8$	$\text{O}_{14}\text{-Ca}_4\text{-O}_{10} \text{ no. 5} = 82.1$	
$\text{O}_{13}\text{-As}_2\text{-O}_{11} \text{ no. 1} = 111.3$	$\text{O}_{10}\text{-Ca}_4\text{-O}_{12} \text{ no. 5} = 74.6$	
$\text{O}_7\text{-As}_2\text{-O}_{11} \text{ no. 1} = 102.0$	$\text{O}_{10}\text{-Ca}_4\text{-O}_9 \text{ no. 3} = 84.7$	

Notes: no. 1 = $x + 1, +y, +z$; no. 2 = $x, +y - 1, +z$; no. 3 = $-x + 1, -y, -z + 1$; no. 4 = $-x + 1, -y + 1, -z + 1$; no. 5 = $-x, -y, -z + 1$.

$[\text{NaO}_6]$ octahedra that form chains along [100]. There are two crystallographically independent $[\text{AsO}_4]$ tetrahedra (centered in As^1 and As^2), which, moreover, have different dimensions (Tables 3 and 4). Although the As-O distances range from 1.65 to 1.72 Å in the $[\text{As}^1\text{O}_4]$ tetrahedra, in the $[\text{As}^2\text{O}_4]$ tetrahedral, these distances show less-significant differences (from 1.66 to 1.69 Å). In both types of tetrahedra, the O-As-O angles are clearly far from the O-T-O inner angle expected for a regular tetrahedron ($\sim 109.47^\circ$). All these features illustrate the distortion of the two $[\text{AsO}_4]$ tetrahedra in the $\text{Ca}_2\text{Na}(\text{HAsO}_4)(\text{AsO}_4) \cdot 6\text{H}_2\text{O}$ structure. Still, the most significant difference between both tetrahedra arises from the fact that one of the O atoms in the $[\text{As}^2\text{O}_4]$ tetrahedra is attached to an H atom at a distance of $\text{O}^{13}\text{-H}^{13} = 0.62$ Å, thereby forming an acidic arsenate HAsO_4^- group. All the O atoms in $[\text{As}^1\text{O}_4]$ are shared with adjacent octahedra. In contrast, in $[\text{As}^2\text{O}_4]$ the O of the hydroxyl apex ($\text{O}^{13}\text{-H}^{13}$) is not shared with other polyhedra, whereas the other three O atoms are linked to adjacent octahedra. The distance, $\text{As}^2\text{-O}^{13} = 1.672$ Å, from the central As to this O atom is similar to the other three $\text{As}^2\text{-O}$ distances. This configuration differs from that observed for other hydrated acidic arsenates like guerinite (Catti and Ferraris 1974), sainfeldite (Ferraris and Abbona 1972), haidingerite ($\text{CaHAsO}_4 \cdot \text{H}_2\text{O}$) (Ferraris et al. 1972), pharmacolite ($\text{CaHAsO}_4 \cdot 2\text{H}_2\text{O}$) (Ferraris et al. 1971), and (Ba,Sr) $\text{HAsO}_4 \cdot \text{H}_2\text{O}$ (Jiménez et al. 2004), in which the O of the hydroxyl apex is at a clearly longer distance from the central As than that of the other three apices in the $[\text{AsO}_4]$ tetrahedron.

Calcium is coordinated with six O atoms to form two crystallographically independent octahedra, $[\text{Ca}^3\text{O}_6]$ and $[\text{Ca}^4\text{O}_6]$. The Ca-O distances within these octahedra show significant differ-

ences among them (Table 3) and the O-Ca-O angles (Table 4) differ significantly from 90 and 180° . These features confirm that both $[\text{CaO}_6]$ octahedra are quite irregular, $[\text{Ca}^4\text{O}_6]$ being more distorted. Figure 8 shows the connection of these $[\text{CaO}_6]$ octahedra with adjacent polyhedra in the structure. As can be observed, two $[\text{Ca}^3\text{O}_6]$ octahedra are edge-sharing through the O atoms O^{11} and $\text{O}^{11} \text{ no. 4}$. In the same way, two $[\text{Ca}^4\text{O}_6]$ octahedra are edge-sharing via $\text{O}^{10} \text{ no. 3}$ and $\text{O}^{10} \text{ no. 5}$. The O^7 atom is simultaneously shared by $[\text{As}^2\text{O}_4]$, $[\text{Ca}^3\text{O}_6]$, and $[\text{Ca}^4\text{O}_6]$. Similarly, O^9 is shared by two octahedra (centered in Ca^3 and Ca^4) and one neighboring As^1 tetrahedron. Moreover, O^{21} links $[\text{Ca}^3\text{O}_6]$ with an adjacent $[\text{As}^1\text{O}_4]$ tetrahedron and O^{14} links $[\text{Ca}^4\text{O}_6]$ with an adjacent $[\text{As}^2\text{O}_4]$ tetrahedron. Finally, the O atom furthest from Ca in each octahedron, O^{17} in $[\text{Ca}^3\text{O}_6]$ and O^{12} in $[\text{Ca}^4\text{O}_6]$, belongs to a water molecule.

Sodium atoms are surrounded by six O atoms to form $[\text{NaO}_6]$ octahedra, which connect the layers formed by $[\text{AsO}_4]$ and $[\text{CaO}_6]$ polyhedra. A scrutiny of Na-O distances and O-Na-O angles (Tables 3 and 4) reveals that these octahedra are closer to a regular octahedron than those coordinating the Ca atoms. The O atoms farthest from the central Na (O^{16} and O^{18}) connect two $[\text{NaO}_6]$ octahedra, which thus form edge-shared chains along [100]. Five of the six O atoms surrounding each Na belong to H_2O molecules (O^{15} , O^{16} , O^{18} , $\text{O}^{16} \text{ no. 6}$, and $\text{O}^{18} \text{ no. 7}$ in Table 3). The remaining O, O^8 , is shared with one $[\text{As}^1\text{O}_4]$ tetrahedron, thereby connecting the $[\text{NaO}_6]$ chains with the (001) layers formed by $[\text{CaO}_6]$ and $[\text{AsO}_4]$ polyhedra.

Figure 9 shows a representation of some typical morphologies exhibited by the $\text{Ca}_2\text{NaH}(\text{AsO}_4)_2 \cdot 6\text{H}_2\text{O}$ crystals. The crystal faces have been indexed according to the unit-cell parameters

conditions, the electrical balance was -1.362 meq/kg, which corresponds to an error of -1.21% . Tables 1 and 2 only display the analytical data corresponding to the end of the experiments (50 days). The complete data set, including all the concentrations and pHs measured at intermediate reaction times, was reported in Rodríguez-Blanco (2006).

Determination of solubility products and saturation indices

The saturation index (SI) is a measure of the supersaturation and is given by

$$SI = \log \frac{\Pi a_i^{v_i}}{K_{sp}} \quad (5)$$

where $\Pi a_i^{v_i}$ stands for the product of ion activities in the actual aqueous solution, v_i is the stoichiometric number of the ion i in the solid formula, and K_{sp} stands for the thermodynamic solubility product of the solid phase, i.e., the equilibrium value of $\Pi a_i^{v_i}$. Obviously, $SI = 0$ reflects equilibrium, $SI < 0$ subsaturation, and $SI > 0$ supersaturation. Therefore, to assess the saturation index with respect to a specific solid phase, one needs to know not only the activities of the participating aqueous ions, but also the solubility product of that solid phase. Unfortunately, the determination of thermodynamic solubility products of Ca arsenates has received little attention and many published data are still open to debate. This occurs because many Ca arsenates are difficult to produce as pure phases. Instead, they are most readily formed in conjunction with other phases such as a mixture of different hydrates, different protonation degrees, etc. Bothe and Brown (1999a) have determined the solubilities of several Ca arsenates including haidingerite ($\text{CaHAsO}_4 \cdot \text{H}_2\text{O}$) and the two polymorphs, guerinite and ferrarisite, of the nonhydrate $\text{Ca}_5(\text{HAsO}_4)_2(\text{AsO}_4)_2 \cdot 9\text{H}_2\text{O}$. Nevertheless, to our knowledge, no data about the solubility products of sainfeldite and, obviously, about $\text{Ca}_2\text{Na}(\text{HAsO}_4)(\text{AsO}_4) \cdot 6\text{H}_2\text{O}$, have been reported. Moreover, the solubility product of the two polymorphs, guerinite and ferrarisite, were determined by far-from-equilibrium precipitation experiments in which an assemblage of two solid phases formed. In such experiments, equilibrium was assumed to occur when, after a while, no change in the aqueous solution composition was observed and the solid phase assemblage remains unaltered. Nevertheless, reaching a true equilibrium situation (at an invariant point) requires a dissolution-recrystallization process involving extremely slow changes, which are difficult to detect at least for short reaction times. In the case of ferrarisite, Bothe and Brown also reported problems of reproducibility in the XRD patterns of the solid phase assemblage. Finally, using the solubility product as determined by Bothe and Brown, the aqueous solution was shown to be undersaturated with respect to guerinite during most of the experiments, which is incompatible with our experimental observations.

Here, the solubility product of guerinite has been estimated assuming that the aqueous solution is at equilibrium with guerinite at the end of the experiments (50 days), which seems to be reasonable if one considers the asymptotic shape of the curve of the analytical data (see Fig. 1). Both the solid phase assemblage and the composition of the aqueous solution remains virtually unchanged during the last 30 days of the experiment. Moreover, the final concentration is virtually the same in the three replicate

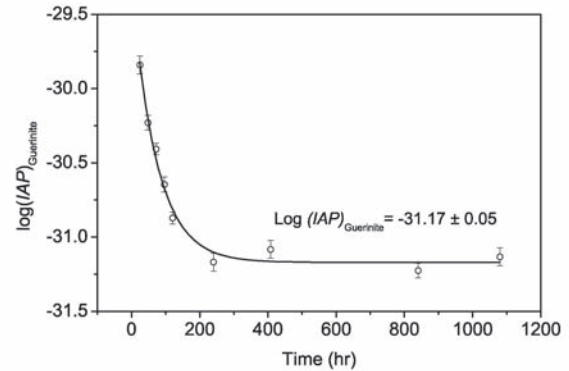


FIGURE 10. Evolution of the ion activity product (logarithm) corresponding to guerinite as a function of time. The data points have been fitted to an exponential decay function. The asymptotic limit is also shown. Parent solution: 25 mM Na_2HAsO_4 . Grain size: $1.0 < \varnothing < 1.5$ mm.

experiments, the relative standard deviation being less than 8%. We have interpreted this to mean that the saturation index with respect to guerinite has to approach zero at the end of the experiments, and that the solubility product can be determined by calculating the asymptotic value of $\Pi a_i^{v_i}$ for prolonged reaction times. For guerinite, the ionic activity product (IAP) is given by the expression:

$$IAP_G = \sum \Pi a_i^{v_i} = a_{\text{Ca}^{2+}}^5 \cdot a_{\text{HAsO}_4^-}^2 \cdot a_{\text{AsO}_4^{3-}}^2 \quad (6)$$

Figure 10 shows the evolution of the logarithm of IAP_G during the experiment performed with 1.0–1.5 mm gypsum grains and a 25 mM Na_2HAsO_4 parent solution. The data points have been fitted to an exponential decay function, the asymptotic limit being -31.17 ± 0.05 . The result corresponds to a solubility product K_{sp} (guerinite) = $10^{-31.17}$, which is slightly lower than that estimated by Bothe and Brown ($10^{-30.69}$). The fact that analogous values have been obtained in the case of the experiments performed with 100, 50, and 20 mM Na_2HAsO_4 parent solutions strongly supports the present estimate. Moreover, this method has proved to be a reliable tool to determine the solubility products of different Ca arsenates at specific pHs. Such is the case of pharmacolite, $\text{CaHAsO}_4 \cdot 2\text{H}_2\text{O}$, whose solubility product was determined at pH 7 (Rodríguez-Blanco et al. 2007) in similar interaction experiments with gypsum.

In the case of sainfeldite, $\text{Ca}_5(\text{HAsO}_4)_2(\text{AsO}_4)_2 \cdot 4\text{H}_2\text{O}$, the determination of the solubility product is more problematic. This mineral has only been observed to form in the experiments carried out with 20 mM Na_2HAsO_4 parent solutions, always in coexistence with the nonhydrate guerinite. In the three replicate experiments, sainfeldite was the last phase that precipitated, i.e., sainfeldite crystallized when the aqueous solution approached saturation with respect to guerinite. Both minerals are different hydrates of the same compound, so that the expression for the two ionic activity products is the same, that is, Equation 6. Obviously, the tetrahydrate can be expected to be stable at a higher temperature than the nonhydrate. Therefore, the fact that both hydrates form together in this experiment indicates that (1) one of the two hydrates is crystallizing in a metastable way, and/or

(2) the transition temperature is very close to 25 °C. On the other hand, the fact that guerinite is the only phase formed in most of the experiments seems to indicate that guerinite is the stable hydrate at 25 °C. Another possibility is that a comparatively lower Ca/As(V) proportion in the aqueous solution favors (from a kinetic point of view) the formation of guerinite or vice versa. In any case, it is reasonable to think that the sainfeldite solubility should be quite similar to the solubility of guerinite and thus the evolution of the saturation index for sainfeldite has to be parallel and probably very close to the evolution of the saturation index for guerinite.

A similar method has been applied to determine the solubility product of $\text{Ca}_2\text{Na}(\text{HAsO}_4)(\text{AsO}_4)\cdot 6\text{H}_2\text{O}$, but in this case, crystallization was carried out by mixing CaCl_2 and Na_2HAsO_4 parent solutions (see experimental section). Equilibrium was assumed to occur after 1500 h of reaction, when the composition of the aqueous solution showed no change with time. The ionic activity product for this new phase is given by the expression:

$$IAP = a_{\text{Ca}^{2+}}^2 \cdot a_{\text{Na}^+} \cdot a_{\text{HAsO}_4^-} \cdot a_{\text{AsO}_4^{3-}} \quad (7)$$

Again, the activities have been calculated by applying PHREEQC to the experimental data (solution pH and analytical concentrations of As, Ca, Na, and Cl). In this case, the equilibrium IAP was $K_{sp} = 10^{-13.83 \pm 0.03}$. The newly obtained solubility products for guerinite and $\text{Ca}_2\text{Na}(\text{HAsO}_4)(\text{AsO}_4)\cdot 6\text{H}_2\text{O}$ can now be incorporated into PHREEQC to calculate the evolution of the saturation indices with respect to these phases during the experiments.

Reaction paths and equilibrium endpoints

Figure 11 shows the evolution of the saturation indices of gypsum and guerinite for the experiments carried out using a 25 mM parent solution and a gypsum grain size in the range $1.0 < \varnothing < 1.5$ mm. These indices have been obtained using a pK_{sp} of 4.58 for gypsum (PHREEQC database) and of 31.17 (this work) and 30.69 (Bothe and Brown 1999a) for guerinite. Moreover, taking into account that in the present experiments the final pH values were around 7.2, the saturation indices of pharmacolite and haidingerite, which usually form below a pH of 7, have also been considered. At the very beginning of the experiment, the aqueous solution is undersaturated with respect to any solid phase, but the fast dissolution of the gypsum grains leads to a dramatic increase of all these saturation indices. As can be observed, the fluid becomes quickly supersaturated with respect to guerinite (note that the first values on the left of the graph do not correspond to 0 h but to 0.5 h of interaction), reaching a maximum ($SI_G \approx 2$) during the first 12 h of the experiment. Afterward, the uninterrupted growth of guerinite leads to a decrease of As(V) concentration in the fluid, and SI_G gradually approaches zero. The saturation index of gypsum evolves differently, approaching equilibrium from undersaturation. As the gypsum grains dissolve, the concentration of Ca and sulfate in the aqueous solution increases, and the gypsum saturation index tends to reach a value close to zero after about 300 h of reaction.

Figure 11 also shows that the fluid is undersaturated with respect to both haidingerite and pharmacolite during the whole reaction time, so that the nucleation of these phases is not pos-

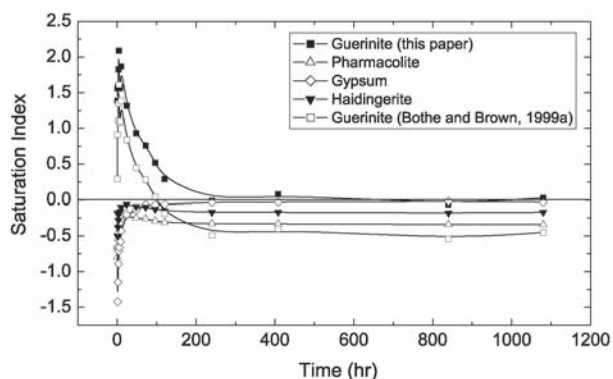


FIGURE 11. Evolution of the saturation index of guerinite, pharmacolite, gypsum, and haidingerite as a function of time. Note that the first values on the left of the graph correspond to 0.5 h of interaction. Parent solution: 25 mM Na_2HAsO_4 . Grain size: $1.0 < \varnothing < 1.5$ mm.

sible. The only mineral that precipitates is guerinite because the aqueous solution becomes highly supersaturated with respect to this phase in the early hours of reaction. The subsequent nucleation and growth of this mineral leads to the removal of Ca and As(V) from the aqueous solution in an uneven proportion, five Ca^{2+} ions for each four arsenate ions, in agreement with solid stoichiometry. As a consequence, the Ca/As(V) ratio in the aqueous solution decreases, which is consistent with a reduction of pH from 9 to ~7.2.

The evolution of the guerinite saturation index observed with a 25 mM solution is quite similar in the experiments performed with 10, 20, 50, and 100 mM Na_2HAsO_4 parent solutions. In all these cases, the saturation index for guerinite is close to zero for prolonged reaction times, the deviations being within the experimental error. The existence of this common endpoint supports the suitability of the solubility product estimated in this paper and confirms that the aqueous solution reaches equilibrium with guerinite at the end of the experiments. In contrast, the end point reached by the gypsum saturation index depends on the parent solution concentration. In the experiments carried out with 2, 5, 10, 20, and 25 mM As(V) parent solutions, equilibrium with gypsum is reached after a more-or-less prolonged reaction time. In contrast, when the initial concentration is higher, the aqueous solution remains undersaturated with respect to gypsum during the whole reaction time (Table 5). This scenario could be explained in view of the SEM observations, which show that, using 50 or 100 mM parent solutions, the gypsum grains become completely covered by guerinite in less than 48 h of reaction. As a consequence, the guerinite precipitate protects the substrate from further dissolution, so that the process stops, at least on the experimental timescale. Obviously, at this stage the system is not at equilibrium, but the term “partial equilibrium” (Helgeson 1968; Prieto et al. 2003) could be used to describe a situation in which the reactive solid (gypsum) becomes isolated from the aqueous solution by a coating of secondary solids that maintain equilibrium with the aqueous phase. In contrast, using 25, 20, or 10 mM parent solutions, the gypsum grains do not become completely covered by the overgrowing crystals and continue to dissolve until equilibrium with respect to both gypsum and guerinite is attained.

TABLE 5. Saturation indices after 50 days of reaction

Parent solution Na ₂ HAsO ₄ (mM)	<i>S_i</i> , gypsum	<i>S_i</i> , guerinite	<i>K</i> (Gy/G)
100	-0.21	0.05	1.5 × 10 ⁷
50	-0.11	0.05	4.5 × 10 ⁷
25	-0.02	0.00	1.5 × 10 ⁸
25 (small size)	-0.02	-0.02	1.5 × 10 ⁸
20	-0.01	-0.03	1.8 × 10 ⁸
10	-0.03	-0.07	1.6 × 10 ⁸
5	0.01	-1.95	1.8 × 10 ¹⁰
2	-0.01	-3.35	3.5 × 10 ¹¹

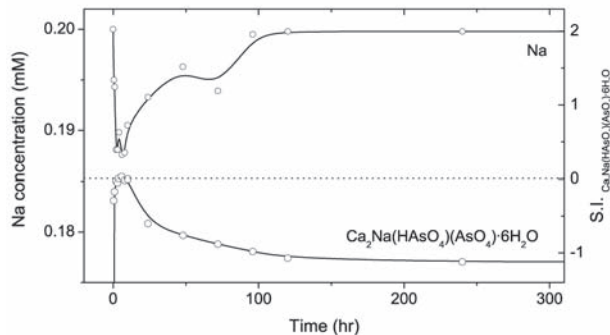


FIGURE 12. Relationship between the evolution of the Na concentration and the saturation index of Ca₂Na(HAsO₄)(AsO₄)·6H₂O. Parent solution: 100 mM Na₂HAsO₄. Grain size: 1.0 < Ø < 1.5 mm.

In the case of the 100 mM parent solution, the evolution of the saturation index of Ca₂Na(HAsO₄)(AsO₄)·6H₂O requires a separate consideration. Figure 12 shows the relationship between the evolution of the Na concentration and the saturation index of this new phase. There is a quick rise of the saturation index during the first 2–8 h of the experiment, which is followed by a simultaneous decrease in Na concentration. The aqueous solution only becomes slightly supersaturated in Ca₂Na(HAsO₄)(AsO₄)·6H₂O during a very short period of time (~6 h), and afterward becomes undersaturated in this phase. This evolution could be explained by the precipitation and subsequent dissolution of Ca₂Na(HAsO₄)(AsO₄)·6H₂O crystals and the corresponding removal-release of Na during the first hours of reaction. Moreover, this result supports the assumption that the solids obtained by mixing of CaCl₂ and Na₂HAsO₄ aqueous solutions correspond to the transitory phase formed using a 100 mM parent solution.

As a final point, it is interesting to discuss the maximum aqueous As(V) concentration that can exist in the presence of gypsum within this pH range. The equilibrium end point would imply simultaneous equilibrium of both guerinite (G) and gypsum (Gy) with the aqueous solution, according to Equation 4. The equilibrium constant for this reaction can be easily derived from the solubility products of both minerals:

$$K_{\text{eq}}(\text{Gy} / \text{G}) = \frac{a_{\text{SO}_4^{2-}}^5}{a_{\text{HAsO}_4^{2-}}^2 \cdot a_{\text{AsO}_4^{3-}}^2} = \frac{a_{\text{Ca}^{2+}}^5 \cdot a_{\text{SO}_4^{2-}}^5}{a_{\text{Ca}^{2+}}^5 \cdot a_{\text{HAsO}_4^{2-}}^2 \cdot a_{\text{AsO}_4^{3-}}^2} = \frac{K_{\text{sp}}^5(\text{Gy})}{K_{\text{sp}}^5(\text{G})} \quad (8)$$

This result means that, at equilibrium, the aqueous activities of SO₄²⁻, HAsO₄²⁻, and AsO₄³⁻ are related in such a way that the ratio *K*(Gy/G) has to be ≈ 1.9 × 10⁸. This condition is reason-

ably satisfied (within the experimental error) at the end of the experiments carried out with 25, 20, and 10 mM parent solutions (see Table 5). However, in the case of experiments carried out with 100 and 50 mM parent solutions, the actual ratio differs by one order of magnitude with respect to the equilibrium value, which confirms the existence of a partial equilibrium situation. Equation 8 also shows that if by some other process, the SO₄²⁻ concentration decreases while equilibrium is maintained for both guerinite and gypsum, then the total concentration of arsenate also decreases due to the solvent-mediated conversion of gypsum to guerinite. For instance, it is easy to calculate using PHREEQC that, if at pH = 7.2 the concentration of sulfate decreases from 30 to 15 mM, then the total concentration of arsenate has to decrease from ~14.6 to ~7.8 mM to maintain equilibrium for both guerinite and gypsum.

Another key factor in determining the removal capacity of the reaction in Equation 4 is the solution pH. At the pH ≈ 7 attained at the end of the experiments, the prevailing arsenate species in the aqueous solution is HAsO₄²⁻, followed by the doubly protonated arsenate ion, H₂AsO₄⁻. The unprotonated arsenate ion, AsO₄³⁻, follows but its concentration is several orders of magnitude lower than that of HAsO₄²⁻. In these conditions, a rise of pH would have the effect of increasing the relative concentration of AsO₄³⁻ at the expense of the concentration of H₂AsO₄⁻. This redistribution, in turn, would lead to an increase in the saturation index of guerinite, so that this phase should precipitate to restore equilibrium. For instance, if the pH increases from 7 to 9, the total concentration of arsenate has to decrease from ~10 to ~2 mM to maintain equilibrium for both guerinite and gypsum. The removal of arsenate is considerably more effective at pH > 9. However, under such conditions, which are beyond the scope of the present work, other Ca arsenates that are less soluble than guerinite would precipitate. Future papers will deal with this matter.

The interaction of As(V)-bearing aqueous solutions with gypsum at a starting pH of ~9 results in surface precipitation of guerinite, sainfeldite, and in some cases Ca₂Na(HAsO₄)(AsO₄)·6H₂O, a new arsenate. These three solid phases are characterized by the simultaneous presence of HAsO₄²⁻ and AsO₄³⁻ groups in their structures, which is explainable as crystallization occurs within a pH range in which both HAsO₄²⁻ and AsO₄³⁻ ions are available in the aqueous solution. This phenomenon leads to a decrease in the As(V) concentration in the aqueous phase to reach values (~15 mM) controlled by the solubility of these solid phases at the final pH (~7.2). This concentration could be further reduced by buffering the pH to 8–9 and/or in the presence of a sink for sulfate, but a value of ~1 mM seems to be the minimum value attainable by precipitation of guerinite. As expected, this concentration is extremely high from the perspective of water quality and thus gypsum does not seem to be a suitable remediation tool in this pH range. However, the nature, solubility, and crystallization behavior of the solid phases that precipitate in this pH range needed to be investigated to get a better understanding of the As(V) behavior in aqueous environments.

ACKNOWLEDGMENTS

This work was supported by the Ministry of Education and Science of Spain (Grant CGL2004-02501). We thank J. Pope and other anonymous reviewers for their insightful comments. Drafts of this manuscript were much improved by the careful reviews of the associate editor Richard Wilkin.

REFERENCES CITED

- Andara, A.J., Heasman, D.M., Fernández-González, A., and Prieto, M. (2005) Characterization and crystallization of the $\text{Ba}(\text{SO}_4)_2\text{SeO}_4$ solid solution. *Crystal Growth and Design*, 5, 1371–1378.
- Beurskens, P.T., Admiraal, G., Beurskens, G., Bosman, W.P., Garcia Granda, S., Gould R.O., Smits, J.M.M., and Smykalla, C. (1992) The DIRDIF program system. Technical Report of the Crystallography Laboratory, University of Nijmegen, The Netherlands.
- Bothe, J.V. and Brown, P.W. (1999a) The stabilities of Ca arsenates at 23 ± 1 °C. *Journal of Hazardous Materials*, 69, 197–207.
- (1999b) Arsenic immobilization by Ca arsenate formation. *Environmental Science and Technology*, 33, 3806–3811.
- Brannon, J.M. and Patrick, W.H. (1987) Fixation, transformation, and mobilization of arsenic in sediments. *Environmental Science and Technology*, 21, 450–459.
- Catti, M. and Ferraris, G. (1974) Crystal structure of $\text{Ca}_3(\text{HAsO}_4)_2(\text{AsO}_4)_2 \cdot 9\text{H}_2\text{O}$ (guerinite). *Acta Crystallographica B*, 30, 1789–1794.
- Catti, M., Chiari, G., and Ferraris, G. (1980) The structure of ferrarisite, $\text{Ca}_3(\text{HAsO}_4)_2(\text{AsO}_4)_2 \cdot 9\text{H}_2\text{O}$. Disorder, hydrogen bonding and polymorphism with guerinite. *Bulletin de Mineralogie*, 103, 541–546.
- Donnay, J.D.H. and Harker, D. (1937) A new law of crystal morphology extending the law of Bravais. *American Mineralogist*, 22, 446–467.
- Dowty, E. (1980) Crystal growth and nucleation theory and the numerical simulation of igneous crystallization. In R.B. Hargraves, Ed., *Physics of magmatic processes*, p. 419–485. Princeton University Press, New Jersey.
- Driehaus, W., Seith, R., and Jekel, M. (1995) Oxidation of arsenate(III) with manganese oxides in water-treatment. *Water Research*, 29, 297–305.
- Farquhar, M.L., Charnock, J.M., Livens, F.R., and Vaughan, D.J. (2002) Mechanisms of arsenic uptake from aqueous solution by interaction with goethite, lepidocrocite, mackinawite, and pyrite: An X-ray absorption spectroscopy study. *Environmental Science and Technology*, 36(8), 1757–1762.
- Fernández-González, A., Andara, A., Alía, J.M., and Prieto, M. (2006) Miscibility in the $\text{CaSO}_4 \cdot 2\text{H}_2\text{O}$ - $\text{CaSeO}_4 \cdot 2\text{H}_2\text{O}$ system: Implications for the crystallization and dehydration behavior. *Chemical Geology*, 225, 256–265.
- Fernández-Martínez, A., Román-Ross, G., Cuello, G.J., Turrillas, X., Charlet, L., Jonson, M.R., and Bardelli, F. (2006) Arsenic uptake by gypsum and calcite: modeling and probing by neutron and X-ray scattering. *Physica B*, 385–386, 935–937.
- Ferraris, G. and Abbona, F. (1972) The crystal structure of $\text{Ca}_3(\text{HAsO}_4)_2(\text{AsO}_4)_2 \cdot 4\text{H}_2\text{O}$ (sainfeldite). *Bulletin Societe Francaise Mineralogie Cristallographie*, 95, 33–41.
- Ferraris, G. and Chiari, G. (1970) The crystal structure of CaHAsO_4 (weilite). *Acta Crystallographica B*, 26, 403–410.
- Ferraris, G., Jones, D.W., and Yerkess, J. (1971) Determination of hydrogen atom positions in the crystal structure of pharmacolite, $\text{CaHAsO}_4 \cdot 2\text{H}_2\text{O}$, by neutron diffraction. *Acta Crystallographica B*, 27, 349–354.
- Ferraris, G., Jones, D.W., and Yerkess, J. (1972) A neutron and X-ray refinement of the crystal structure of $\text{CaHAsO}_4 \cdot \text{H}_2\text{O}$ (haindingerite). *Acta Crystallographica B*, 28, 209–214.
- Foster, A.L., Brown, G.E., and Parks, G.A. (1998) Quantitative arsenic speciation in mine tailings using X-ray absorption spectroscopy. *American Mineralogist*, 83, 553–568.
- Frost, R.R. and Griffin, R.A. (1977) Effect of pH on adsorption of arsenic and selenium from landfill leachate by clay minerals. *Soil Science Society America Journal*, 41, 53–57.
- Helgeson, H.C. (1968) Evaluation of irreversible reactions in geochemical processes involving minerals and aqueous solutions. I: Thermodynamic relations. *Geochimica Cosmochimica Acta*, 32, 853–877.
- Jiménez, A., Prieto, M., Salvadó, M.A., and Gracia-Granda, S. (2004) Structure and crystallization behavior of the $(\text{Ba},\text{Sr})\text{HAsO}_4 \cdot \text{H}_2\text{O}$ solid-solution in aqueous environments. *American Mineralogist*, 89, 601–609.
- Jiménez, A., Rodríguez, J.D., Torre-Fernández L., Prieto, M., and Gracia-Granda, S. (2006) Crystal structure of dicalcium sodium monohydrogen diarsenate hexahydrate, $\text{Ca}_2\text{Na}[\text{HAsO}_4][\text{AsO}_4] \cdot 6\text{H}_2\text{O}$. *Zeitschrift für Kristallographie NCS*, 221, 241–242.
- Juillot, F., Ildefonse, Ph., Morin, G., Calas, G., Kersabiec, A.M., and Benedetti, M. (1999) Remobilization of arsenic from buried wastes at an industrial site: mineralogical and geochemical control. *Applied Geochemistry*, 14, 1031–1048.
- Lee, J.S. and Nriagu, J.O. (2007) Stability constants for metal arsenates. *Environmental Chemistry*, 4(2), 123–133.
- Magalhães, M.C.F. (2002) Arsenic: An environmental problem limited by solubility. *Pure and Applied Chemistry*, 74, 1843–1850.
- Manning, B.A. and Goldberg, S. (1996) Modeling arsenate competitive adsorption on kaolinite, montmorillonite, and illite. *Clays and Clay Minerals*, 44, 609–623.
- Nishimura, T., Tozawa, K., and Robins, R.G. (1983) The Calcium-Arsenic-Water System. Proceedings MMII/Aus IMM Joint Symposium, Paper JD 2-1, p. 105–120. Sendai, Japan.
- Nishimura, T., Robins, R.G., and Twidwell, L.G. (2000) The removal of arsenic from hydrometallurgical processes and effluent streams. In M.A. Sánchez, F. Vergara, and S.H. Castro, Eds., *Waste treatment and Environmental Impact in the Mining Industry Proceedings of the 5th International Conference on Clean Technologies for the Mining Industry*, vol. 1, p. 131–141. Santiago, Chile.
- Oelkers, E.H. (1996) Physical and chemical properties of rocks and fluids for chemical mass transport calculations. In P.C. Lichtner, C.I. Steefel, and E.H. Oelkers, Eds., *Reactive Transport in Porous Media*, 34, p. 131–191. Reviews in Mineralogy, Mineralogical Society of America, Chantilly, Virginia.
- O'Reilly, S.E., Strawn, D.G., and Sparks, D.L. (2001) Residence time effects on arsenate adsorption/desorption mechanisms on goethite. *Soil Science Society America Journal*, 65, 67–77.
- Parkhurst, D.L. and Appelo, C.A.J. (1999) User's Guide to PHREEQC (Version 2)—A Computer Program for Speciation, Batch-Reaction, One-dimensional Transport and Inverse Geochemical Calculations. U.S. Geological Survey Water Resources Investigations Report 99-4259, U.S. Geological Survey, Washington, D.C., 310 p.
- Pierce, M.L. and Moore, C.B. (1982) Adsorption of arsenite and arsenate on amorphous iron hydroxide. *Water Research*, 16, 1247–1253.
- Prieto, M., Fernández-González, A., and Martín-Díaz, R. (2002) Sorption of chromate ions diffusing through barite-hydrogel composites: Implications for the fate and transport of chromium in the environment. *Geochimica Cosmochimica Acta*, 66, 783–795.
- Prieto, M., Cubillas, P., and Fernández-González, A. (2003) Uptake of dissolved Cd by biogenic and abiogenic aragonite: A comparison with sorption on calcite. *Geochimica Cosmochimica Acta*, 67, 3859–3869.
- Robins, R.G. (1981) The Solubility of Metal Arsenates. *Metallurgical Transaction B: Process Metallurgy*, 12, 103–109.
- Rodríguez-Blanco, J.D. (2006) Interaction of As(V) with gypsum at different pH ranges. Ph.D. thesis, Universidad de Oviedo, Spain.
- Rodríguez-Blanco, J.D., Jiménez, A., and Prieto, M. (2007) Oriented overgrowth of pharmacolite on gypsum. *Crystal Growth and Design*, 7, 2756–2763.
- Roman-Ross, G., Charlet, L., Cuello, G.J., and Tisserand, D. (2003) Arsenic removal by gypsum and calcite in lacustrine environments. *Journal de Physique*, IV 107, 1153–1156.
- Smedley, P.L. and Kinniburgh, D.G. (2002) A review of the source, behavior and distribution of arsenic in natural waters. *Applied Geochemistry*, 17, 517–568.
- Sposito, G. (1986) Distinguishing adsorption from surface precipitation. In J.A. Davis and K. Hayes, Eds., *Geochemical Processes of Mineral Surfaces*, 323, 217–228. ACS Symposium Series, Oxford University Press, New York.
- Swash, P.M. and Monhemius, A.J. (1995) Synthesis, characterization and solubility testing of solids in the Ca-Fe-AsO₄ system. In T.P. Hynes and M.C. Blanchette, Eds., *Sudbury '95—Mining and the Environment*, CANMET, p. 17–28. Ottawa, Canada.
- Twidwell, L.G., McCloskey, J., Miranda, P., and Gale, M. (1999) Technologies and potential technologies for removing arsenic from process and mine water. In I. Gaballah, J.P. Hager, and R. Solozabal, Eds., *Rewas'99, Global Symposium on Recycling, Waste Treatment and Clean Technology*, p. 1715–1726. The Minerals, Metals and Materials Society, Warrendale, U.S.A.
- Vaughan, D.J. (2006) Arsenic. *Elements*, 2, 71–75.

MANUSCRIPT RECEIVED JULY 16, 2007

MANUSCRIPT ACCEPTED DECEMBER 27, 2007

MANUSCRIPT HANDLED BY RICHARD WILKIN